



HAL
open science

Spatiotemporal Evolution of the Seismicity in the Alto Tiberina Fault System Revealed by a High-Resolution Template Matching Catalog

David Essing, Piero Poli

► **To cite this version:**

David Essing, Piero Poli. Spatiotemporal Evolution of the Seismicity in the Alto Tiberina Fault System Revealed by a High-Resolution Template Matching Catalog. *Journal of Geophysical Research : Solid Earth*, 2022, 127, 10.1029/2022JB024845 . insu-03861044

HAL Id: insu-03861044

<https://insu.hal.science/insu-03861044>

Submitted on 24 Mar 2023

HAL is a multi-disciplinary open access archive for the deposit and dissemination of scientific research documents, whether they are published or not. The documents may come from teaching and research institutions in France or abroad, or from public or private research centers.

L'archive ouverte pluridisciplinaire **HAL**, est destinée au dépôt et à la diffusion de documents scientifiques de niveau recherche, publiés ou non, émanant des établissements d'enseignement et de recherche français ou étrangers, des laboratoires publics ou privés.

Copyright

JGR Solid Earth

RESEARCH ARTICLE

10.1029/2022JB024845

Key Points:

- Using template matching we detect nearly half-million earthquakes over ~3 years in the Alto Tiberina Fault system
- The application of spatiotemporal analysis reveals a variable style of seismicity in the fault system
- Detection and analysis of repeating earthquakes do not support occurrence of creep along the deep part of the low angle normal fault

Supporting Information:

Supporting Information may be found in the online version of this article.

Correspondence to:

D. Essing,
david.essing@univ-grenoble-alpes.fr

Citation:

Essing, D., & Poli, P. (2022). Spatiotemporal evolution of the seismicity in the Alto Tiberina Fault system revealed by a high-resolution template matching catalog. *Journal of Geophysical Research: Solid Earth*, 127, e2022JB024845. <https://doi.org/10.1029/2022JB024845>

Received 26 MAY 2022
Accepted 3 OCT 2022

Author Contributions:

Conceptualization: David Essing, Piero Poli
Formal analysis: David Essing, Piero Poli
Investigation: David Essing, Piero Poli
Methodology: David Essing, Piero Poli
Supervision: Piero Poli
Validation: David Essing, Piero Poli
Visualization: David Essing
Writing – original draft: David Essing
Writing – review & editing: David Essing, Piero Poli

© 2022. American Geophysical Union.
All Rights Reserved.

Spatiotemporal Evolution of the Seismicity in the Alto Tiberina Fault System Revealed by a High-Resolution Template Matching Catalog

David Essing¹  and Piero Poli^{1,2} 

¹ISTerre Institut des Sciences de la Terre, CNRS, Université Grenoble Alpes, Gières, France, ²Dipartimento di Geoscienze, Università degli Studi di Padova, Padova, Italy

Abstract The Alto Tiberina Fault system, located in the Northern Apennines (Italy), consists of a low angle normal fault (LANF) which radiates micro-seismicity that can be explained by continuous creep. On top of the LANF, a network of syn- and antithetic high angle faults frequently hosts seismic swarms, one of which has been associated with a transient aseismic deformation signal. To study in detail the seismicity and its relationships with aseismic deformation processes occurring in this fault system, we apply template matching on seismic data recorded at an array of borehole stations, to derive a high-resolution earthquake catalog. Thanks to the additionally detected events, we are able to reveal time periods of increased spatial- and temporal clustering during an aseismic deformation event. This reflects the complex evolution of aseismic slip together with the complexity of the shallow fault system. Along the LANF, we observe a bimodal type of seismicity, with diffuse seismicity active continuously, and short-lived bursts of seismicity that could indicate rapid fluid releases. We additionally identify repeating earthquakes. These events not necessarily match a simple creep model and therefore open the possibility for new models to explain the seismicity along the LANF.

Plain Language Summary The existence of normal faults with small dip angles is suggested to be unlikely by regular frictional models. Nevertheless, low angle normal faults are documented in several parts of the world and understanding their way of releasing accumulated strain is fundamental, to infer whether or not they are capable to host large devastating earthquakes. The Alto Tiberina Fault system hosts one of the best instrumented low angle normal faults in the world. To better understand the different mechanisms responsible for the seismicity originating from these faults, we applied a technique that allows the detection of new earthquakes that are similar to the ones we already know. Applying this technique helps to increase the number of detected earthquakes, thus helping to better characterize the behavior of the overall seismicity in space and time. The analysis of the detected seismicity suggest that the earthquakes radiated from the high angle faults are driven by short-lived processes lasting several days up to weeks. The analysis of the earthquakes radiated from the Alto Tiberina low angle fault reveals continuous processes acting within this region. Additionally, the low angle fault radiates earthquakes in extremely short time intervals of minutes from nearby areas, which could suggest the effect of fluids.

1. Introduction

Low angle normal faults (LANF) are intriguing geological structures found in extensional tectonic regimes (Wernicke, 1995). Those structures are normal faults with a dip angle lower than 30°, which should inhibit frictional fault reactivation under the well accepted Anderson-Byerlee theory of faulting (Byerlee, 1978; Collettini, 2011). Nevertheless, seismically active LANFs are found in several locations around the world, such as in Greece in the Gulf of Corinth (Rietbrock et al., 1996), in Papua New Guinea in Mai'iu (Abers et al., 1997; Biemiller et al., 2020) and in Italy along the Apennines (Chiaraluce et al., 2007). Observations of seismic activity along LANFs raises the question whether these faults are capable of producing moderate-to-large magnitude earthquakes, or whether other deformation mechanisms accommodate the extension (e.g., Collettini, 2011; Wernicke, 1995).

A well-studied LANF is the Alto Tiberina Fault (ATF) located in the Apennines (Figure 1), which is thought to accommodate large portions of the overall tectonic extension of ~3 mm/yr within the region (Serpelloni et al., 2005). The structure of this fault is well characterized by several seismological studies, as deep seismic reflection profiles (Barchi et al., 2003), controlled source seismic imaging (Mirabella et al., 2004), and

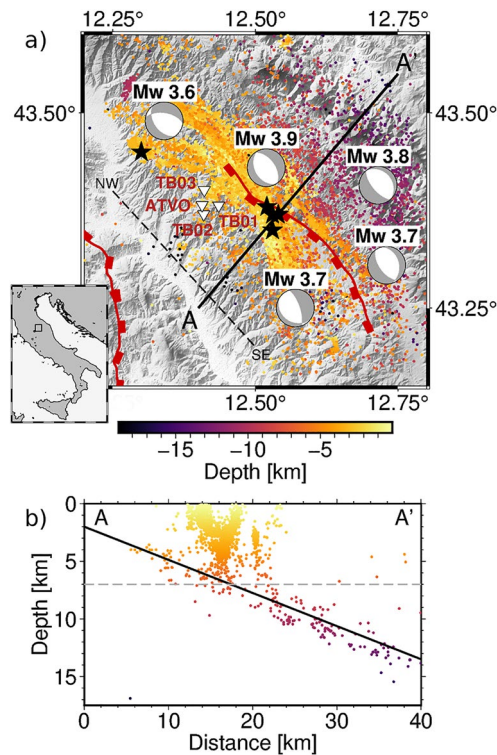


Figure 1. (a) Map of the study area in Italy. Triangles show the locations of the borehole stations (TB0X) and one surface station (ATVO). To indicate depth, the seismicity is color-coded. The locations of the five largest events during the study period are indicated by black stars, while their focal mechanisms are indicated by beach-balls. Red lines indicate the surface traces of the LANF (SW) and the Gubbio fault (central part) and are taken from v. Gessel et al. (2021). Dashed line indicates the projection along strike for Figure 3. (b) Cross-section of the study area as indicated in (a). Solid line indicates the fault surface of the LANF while the dashed line indicates the separation depth used in this study.

seismic tomography (e.g., Chiarabba & Amato, 2003; Pauselli et al., 2006; Piana Agostinetti et al., 2017). Further studies characterized the ATF with gravity (Boncio et al., 2000), magnetic (Collettini & Barchi, 2002), and heat flow measurements (Mirabella et al., 2004). These studies reveal a NNW trending major fault dipping 15°–20° from the surface to ~12–14 km depth. Below 4 km the fault plane is highlighted by micro-seismicity within a 500–1,000 m thick fault zone (Chiaraluce et al., 2007). This micro-seismicity was initially observed at a constant rate (Chiaraluce et al., 2007), while recent research highlighted a variable rate of seismicity along the shallow parts of the LANF, connected with the activity in the HW (Vuan et al., 2020).

The hanging wall (HW) of the LANF is dominated by several syn- and anti-thetic splay faults with high dipping angles of 50°–60°. The largest structure is the Gubbio fault showing a listric geometry, dipping 40°–60° at shallow depths and bending to 10°–15° below depths of 3–4 km (Mirabella et al., 2004). Between 3 and 6 km depth, the HW is characterized by high V_p - V_s ratios, indicative of high pore-fluid pressure (Chiarabba & Amato, 2003; Piana Agostinetti et al., 2017). This layer consists of Mesozoic carbonates and Triassic evaporitic rocks and hosted several swarm-type seismic sequences in 2001 (Chiaraluce et al., 2007; Piana Agostinetti et al., 2017; Piccinini et al., 2003), 2010, and 2013–2014 (Valoroso et al., 2017). Rare is the occurrence of events larger than $M_w \sim 4$. Among these events, the better recorded occurred in 1984 a M_w 5.6, and probably ruptured a fault in the HW (Collettini et al., 2003; Haessler et al., 1988; Pucci et al., 2003). Historical events with $M > 6$ in 1352, 1751, and 1781 are also reported for the area but not directly linked to the ATF (Valoroso et al., 2017).

Focusing on the mechanical behavior of the ATF, several studies (Anderlini et al., 2016; Chiaraluce et al., 2014; Collettini et al., 2011; Hreinsdóttir & Bennett, 2009; Vadacca et al., 2016) proposed that the extension in the area is accommodated to some degree by creep along the LANF. Combining a block modeling approach with GPS velocities measured at a dense GPS network in the area, Anderlini et al. (2016) inferred partial creep of 1.7 mm/yr along the LANF, with several asperities being locked. Later, the geodetic data analysis of Gualandi et al. (2017) revealed a small transient deformation equivalent to a M_w 4.8 overlapping in time and space with the swarm-like seismic sequence reported for 2013–2014.

Gualandi et al. (2017) identified the slip to occur within shallow depths between 0 and 5 km, along two high-angle faults within the HW of the LANF. The swarm-like seismic activity linked with the transient deformation was studied using a high-resolution earthquake catalog from 2010 to 2014 (Valoroso et al., 2017). This study revealed a complex mixed mode seismicity (Valoroso et al., 2017). More recently, Vuan et al. (2020) used template matching (TM) to better characterize the seismicity adjacent to the LANF surface and found several productive clusters indicating a time intermittent activity rate, indicative of an interaction with $M > 3$ earthquakes and slow deformation occurring within the HW.

Despite the studies cited above, several questions regarding the mechanical behavior of the ATF-system remain open. A first open question is how the accommodated stress within the study area is released, either by continuous deformation along the LANF (Anderlini et al., 2016), transient deformation within the HW (Gualandi et al., 2017), or a complex interplay of both mechanisms (Vuan et al., 2020). Another open question concerns the driving mechanism of the swarm-like seismic sequences within the HW, and more in particular if seismicity is controlled by aseismic slip, fluids or elastic interaction (Chiaraluce et al., 2007; Chiodini et al., 2004; Duverger et al., 2018; Gualandi et al., 2017; Martínez-Garzón et al., 2021; Ruhl et al., 2016; Valoroso et al., 2017).

To tackle the aforementioned challenges, we first derive a new high-resolution catalog of small earthquakes. This extended catalog is produced using a TM approach (Gibbons & Ringdal, 2006) applied to an array of borehole stations (Chiaraluce et al., 2014) recording high-frequency (sampling rate of 500 Hz) and low noise data (Figure 2a). Starting from an initial catalog of ~30,000 earthquakes we detect more than 400,000 new events

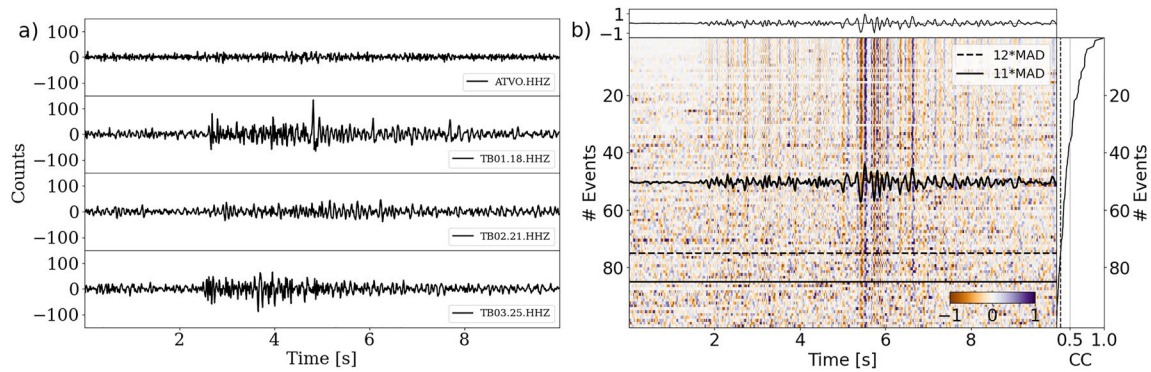


Figure 2. (a) Waveforms of a $M \sim -1.8$ event, recorded at the vertical components of the stations indicated in Figure 1a. The event occurred on 2013-04-21T20:15:15 northeast of the station array. (b) Waveforms of all detections made by a template event (2013-12-23T17:02:05, $M_w = -0.98$), normalized by their absolute maximum (recorded at TB01.BHZ). The waveform of the template event is indicated in the upper panel. Right panel shows the average correlation coefficient (CC) between the new detections and the template event. As indicated in the right panel, the normalized waveforms are sorted by a decreasing ratio between the average correlation coefficient and the median absolute deviation (MAD) of the daily average correlation coefficient. The horizontal dashed and solid lines indicate ratios of 12 and 11, respectively. A stack of the normalized waveforms of all events is indicated at Event 50 in black.

with magnitude as low as -2 . We further analyze the detected seismicity in terms of event interaction in time and space, and systematically search and model repeating earthquakes (RE), to infer the role of creep along the LANF (Nadeau & McEvilly, 1999). We finally propose models to reconcile the observed seismological behavior and reveal a complex coexistence of different processes along the ATF fault system.

2. Detection of the Seismicity

To enhance the detection of small earthquakes and improve the time resolution of the seismicity in the study area, we make use of TM (Gibbons & Ringdal, 2006) and apply this array processing approach to data recorded at a network of seismic borehole stations as seen in Figure 1a (Chiaraluze et al., 2014). Our analysis covers a time period from July 2012 to December 2015, which includes a transient aseismic deformation signal (Gualandi et al., 2017) that coincides with a major earthquake swarm (Valoroso et al., 2017).

The seismic network used in this study is installed within three boreholes (Figure 1a) two of them having one surface station and one deep station (stations TB01 and TB02), and one borehole with a surface station plus 3 stations at different depths inside the borehole (station TB03). After quality control of the data, including visual inspection in time and frequency domain, we noticed that surface stations show a general high level of noise with a daily variation. Additionally, the continuous data is contaminated by artifacts and spikes. As these spurious signals are not consistent over different stations, we speculate that they originate from a source close to the sensor, probably related directly to the sensor or the digitizer. We further observe that the deepest stations are much more sensitive to small magnitude events, as illustrated in Figure 2a. We thus focus our analysis on four seismometers (3-components each) located at depth (TB01 (180 m), TB02 (210 m), TB03 (150 m), and TB03 (250 m)) with interstation distances ranging from 2.4 to 3.4 km. For all mentioned stations the data was sampled at 500 Hz throughout the duration of the study period.

The continuous data is analyzed using a TM technique (Gibbons & Ringdal, 2006), which has been shown optimal to detect small signals with extremely low signal to noise ratios (SNR) (e.g., Beaucé et al., 2018; Beaucé et al., 2019; Sánchez-Reyes et al., 2021). In TM, the P and S waveforms of known earthquakes (templates) are component-wise extracted with a distinct window length (see below) and then correlated with continuous data. At each time step, the correlation coefficient (CC) between the template window and the continuous data is calculated. This is done for each station and component, and finally averaged over all used components. A new detection is defined when the averaged CC reaches a certain threshold (e.g., Beaucé et al., 2018; Beaucé et al., 2019; Sánchez-Reyes et al., 2021). Here, this threshold is set to be 10 times the median absolute deviation (MAD) of the averaged CC for a specific template on a certain day.

To prepare TM, the first step of our data processing consists in preparing the continuous seismic data. The daily traces are synchronized to provide seismograms of 24 hr starting at midnight. The data is then detrended, filtered

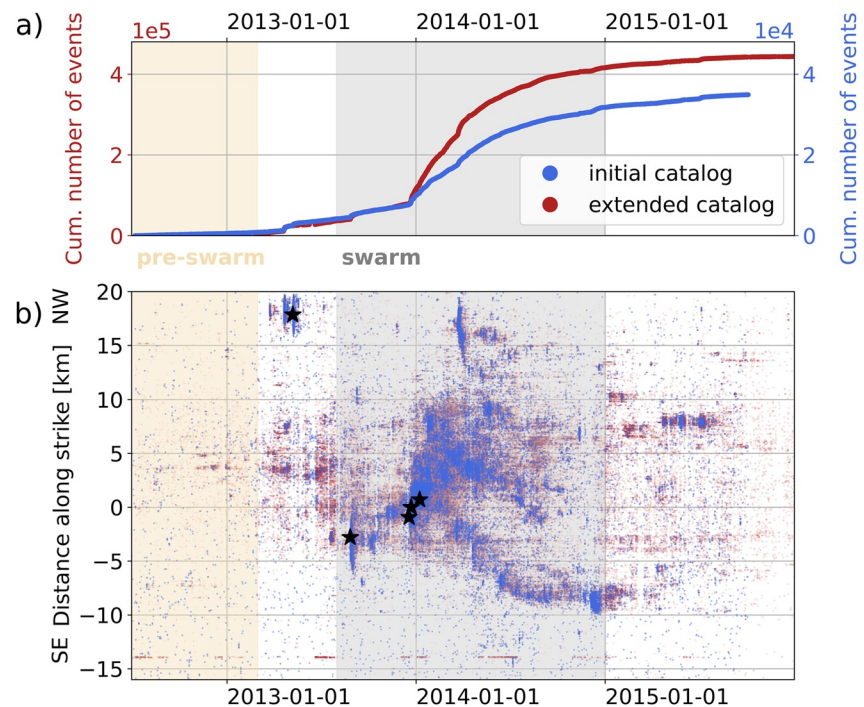


Figure 3. (a) Cumulative number of events for the initial (blue) and the extended (red) catalog. Note the two different scales. Two distinct time periods (pre-swarm and swarm) of distinctive style of seismicity are indicated. (b) Space-time evolution along strike as indicated in Figure 1a, for the initial (blue) and the extended (red) catalog. Black stars mark the five largest events within the study period (see Figure 1a).

from 5 to 49 Hz using a Butterworth filter, and resampled at 100 Hz. The frequency band used here differs from earlier studies within the study area (e.g., Vuan et al., 2020) and permits the detection of low magnitude events (Cabrera et al., 2022), as they are expected to have better SNR at higher frequencies (e.g., Abercrombie, 2021). Furthermore, by using 5 Hz as the lower corner frequency, we avoid systematically observed local noise which is strong in the frequency range from 1 to 5 Hz (Cabrera et al., 2022; Latorre et al., 2014; Poli et al., 2020; Sánchez-Reyes et al., 2021).

In a second step, we extract the potential templates from the continuous data. For this we use the earthquakes from the catalog of Valoroso et al. (2017) (Figure 1a; Figure 3). For the time period (July 2012 until December of 2015) the catalog contains 34,923 events, which are precisely relocated using a double difference approach (Valoroso et al., 2017). In our work, we define a template as 1.2 s long P and S waveform, starting 0.4 s before the theoretical arrival time at each seismometer. The arrival time at each seismometer is predicted with a local 1D velocity model, which permits the extraction of seismic phases at each station (Chiaraluce et al., 2007; Table S1 in Supporting Information S1). P waveforms are extracted from the vertical seismometer component, while the S waveforms from the horizontal components. For each potential template we calculate the root-mean-square (rms) amplitude within a noise window (1.2 s long time window previous to the P wave arrival) and relate this to the rms amplitude within the P and S wave windows to obtain the SNR for each template. Only templates with a SNR >3 at more than 8 seismometer components are retained for further analysis. This step reduces the number of templates for the final run to 28,903.

We then use each template to scan the daily continuous data with a sliding window of one sample. This computation implies the calculation of $\sim 10^{15}$ correlations. To perform this large analysis, we use the Fast Matched-Filter (FMF) code of Beaucé et al. (2018) based on a parallel GPU framework. The processing required 2,800 hr of computation, performed using a single NVIDIA Tesla V100 GPU with NVLink. For each template we obtain daily traces of CC averaged over all seismometer components, which are then used to extract new detections. To identify new detections, we first estimate the MAD for each daily trace of average CCs, and then define a new detected event when the averaged CC at a sample exceeds the daily MAD by a factor of 10. This preliminary threshold was chosen from tests made with a subset of data, using low SNR templates. With these parameters

we obtain a first set of detections, which includes redundant ones (e.g., new detections identified by multiple templates). This redundancy results in event detections with an interevent time smaller than the template window length (1.2 s). Therefore, we decluster this first set of detections using the interevent arrival time at the seismometer network. In this study we retain events with an average interevent arrival time at the network larger than 1.2 s, which corresponds to the window length of the template. This approach allows to detect events with interevent times even below 1.2 s, if the hypo-central distances between these events are large enough. Within a group of redundant detections, the CC ranges from ~ 0.2 to values of up to one if an auto-detection is included. In each group of redundant detections, we retain only the one with the highest CC for the final extended catalog. After declustering the extended catalog consists of 630,265 detected events, that is 21 times the number of events within the initial catalog.

Each newly detected event is assigned to the location of the template which detected it (Valoroso et al., 2017). We estimate the magnitude of a newly detected event by measuring the ratio of the waveform amplitudes between the template and the newly detected event (Cabrera et al., 2022; Peng & Zhao, 2009). The ratio is taken from the mean value of the absolute signal within a window length of 1.2 s during the P-arrival on every component. Then, the new magnitude is estimated by adding the logarithm to the base of 10 of the median ratio of all components to the template's magnitude. This approach assumes a change of 10 in the amplitude as a change of 1 unit in magnitude (Cabrera et al., 2022; Frank et al., 2017; Peng & Zhao, 2009).

We subsequently perform quality control on the extended catalog, to ensure that only real detections of good quality are included. This step involves visual inspection of events detected by single templates (Figure 2b). We thus plotted 10 s of the waveforms for all detections made by one template sorted by a decreasing CC to MAD ratio as seen in Figure 2b. New detected events above the dashed line have a ratio >12 , while detections above the solid line have a ratio >11 . From Figure 2b, we see clear P wave arrivals for the first 30 detections, while the quality of detected signals reduces around detection number 40. The S wave arrivals are generally more prominent and can be seen for almost all detections, with significant quality reduction below a ratio of 11.

We performed the aforementioned procedure of visual inspection on randomly chosen families. The approach led us to the choice of retaining only detections with a CC to MAD ratio >12 as new events which is in good agreement with other studies based on TM (Sánchez-Reyes et al., 2021; Shelly, 2020). This choice leads to a final catalog of 447,834 events which is an extension of the initial catalog (34,923 events) by a factor of ~ 12 , in agreement with studies from other areas using a similar approach (e.g., Gibbons & Ringdal, 2006; Sánchez-Reyes et al., 2021; Shelly, 2020).

3. The Extended Seismic Catalog

From 28,903 templates we were able to retrieve 447,834 events. A comparison of the time and space evolution of the new events is reported in Figure 3, together with the initial catalog (Valoroso et al., 2017). The extended catalog contains one order of magnitude more events than the initial one, while it preserves a similar time evolution for the cumulative number of events (Figure 3a). This is seen as a first order quality estimate, as it reproduces the overall evolution of the seismicity.

The fact that the number of new detections is not constant over the analyzed time is an intriguing characteristic of the extended catalog (Figure 3a). The cumulative event number of both catalogs follows the same time evolution in the first part of the studied period, up to December 2013, with the extended catalog containing 10 times more events than the initial one (Figure 3a, note the different y-axis). However, in January 2014, the ratio of new events to templates events exceeded 10 (Figure 3a). To ensure that this evolution of the cumulative event number is not related to changes in data quality we inspected the continuous data related to the days in late December 2013 without finding anomalies. This increment is thus reflecting a true seismicity increase. Indeed, the extended catalog has a potential time resolution below 1.2 s, which allows to resolve events with very short interevent times (Figure S1 in Supporting Information S1), of even less than 2 s (Figure S2 in Supporting Information S1). This aspect has a significant impact on the increment factor we obtained, which allows to resolve an extremely high seismicity rate as in January 2014 (Figure 3), and therefore enables us to resolve the small-scale spatio-temporal evolution.

We additionally observe 4,157 periodically activated events (Figure S3a in Supporting Information S1) at along strike distance approximately -15 km (Figure 3b) within the extended catalog. These events were detected by

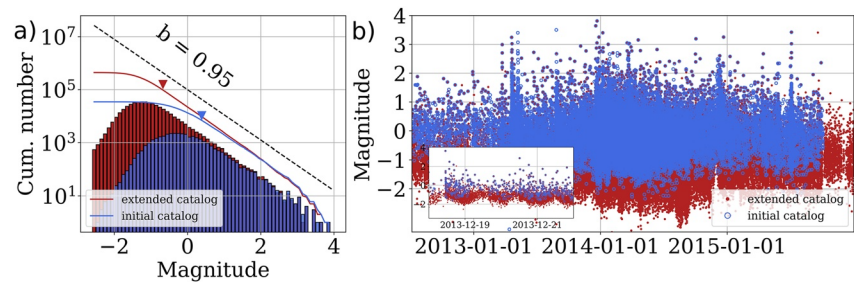


Figure 4. (a) Frequency-magnitude distribution for the initial (blue) and the extended (red) catalog. Continuous lines indicate the cumulative distributions while the dashed line indicates the b -value of the initial catalog (Valoroso et al., 2017). Triangles indicate the magnitude of completeness estimated following the approach of Herrmann and Marzocchi (2021). (b) Magnitudes as a function of time for the initial (blue) and the estimated magnitudes for the extended (red) catalog. Inset: As (b), for the time period from 2013-12-18 to 2013-12-22.

templates located at shallow depths (between 0.09 and 1.9 km) within a small region at the southern end of the Gubbio basin close to a cement factory. The waveforms of these events (Figure S3b in Supporting Information S1) consist mainly of low frequency signals similar to the events observed by Latorre et al. (2014). In the following analysis, we removed these events, as they can be considered as a nuisance for earthquake related studies (Gulia & Gasperini, 2021). However, human made signals can potentially be used to monitor changes in physical properties in the fault system, using recently proposed correlation approaches (Pinzon-Rincon et al., 2021).

In Figure 4a we compare the frequency-magnitude distribution of the extended and the initial catalog (Valoroso et al., 2017). Even though both catalogs share a similar slope, the estimated magnitude of completeness (Herrmann & Marzocchi, 2021) decreased from 0.39 for the initial catalog to -0.67 for the extended one (Figure 4a).

Figure 4b further compares the estimated magnitudes with the magnitudes of the initial catalog as a function of time. This figure again reveals the improved magnitude resolution of the extended catalog, and its capability to resolve in detail the large number of events associated with each burst of seismicity (Figure 4b). There is however in both catalogs a daily evolution of minimum resolved magnitude, with smaller magnitude events better detected during nighttime (Figure 4b inset). This phenomenon was already seen in another TM study (Sánchez-Reyes et al., 2021) and might be due to daily anthropogenic noise variation (Poli et al., 2020). This should be considered for example, while performing statistical analysis of the seismicity (e.g., Marsan & Nalbant, 2005). A further issue in the presented approach is the limitation to a borehole station network consisting of only four sensors (12 channels). During periods when no data is available for more than one station, the results of TM are less reliable, and are therefore not included within the extended catalog presented here. Especially during early 2013, Figures 3b and Figure 4b show several gaps of data indicated by vertical empty lines.

The results of the extended catalog can be partially compared with a previous study (Vuan et al., 2020), where the authors applied TM using events nucleating within 1,500 m from the assumed ATF surface to detect $\sim 16,000$ earthquakes within our study period. With the TM approach presented here we are able to detect 32,158 events nucleating in the same fault volume, which is more than twice the number of events detected by Vuan et al. (2020). We postulate that the reason for the improved performance in this study is related to the use of a higher frequency band and the higher sampling rate, which allows to better detect small magnitude events. Additionally, the borehole data used in this study seems to be less sensitive to noise (Chiaraluce et al., 2007), and therefore better resolve the micro-seismicity nucleated from the deeper parts of the LANF.

Even though we are able to detect a large amount of new seismic events from areas where templates are available, the inherent disadvantage of TM is its blindness in areas where no seismicity, or any other signal was previously identified. This represents the weak point of TM compared to other detection methods like used by Majstorović et al. (2021) which do not rely on previously characterized events from distinct areas. The extended catalog is available in electronic format (see Data Availability Statement).

4. Time and Space Evolution of the Seismicity

In the following, we use the extended catalog containing 443,677 events (without the 4,157 human induced sources) to derive new insights about the dynamics of the seismicity, to shed light on deformation processes and infer mechanical properties of the ATF fault system.

4.1. Time and Space Clustering of the Seismicity

We begin the analysis by assessing the interaction in time and space between seismic events. The presence (absence) of earthquakes clustering provides fundamental insights into the dynamics of seismicity and rheological properties of fault systems, as revealed from seismological studies (Liu et al., 2022) and numerical modeling (Dublanche et al., 2013). The simplest mechanism of time and space clustering of earthquakes is through interactions between events during co- and post-seismic processes, like static or dynamic stress transfer triggering (Freed, 2005) or afterslip (Perfettini & Avouac, 2004), with additional modulation related to the asperity density (Dublanche et al., 2013). Alternatively, enhanced interaction can result from external forcing as slow aseismic deformation (Frank et al., 2016; Lengliné et al., 2017; Poli et al., 2022), fluid fracturing (Obara, 2002; Seno & Yamasaki, 2003) or coupled fluid and rock interaction (Shelly et al., 2006), in complex fault systems (e.g., Dublanche et al., 2013).

We start by dividing the seismicity into pre-swarm (beginning of the catalog until 2013-03-01) and swarm (2013-08-01 until 2014-12-31) periods (Figure 3), guided by the results of Gualandi et al. (2017) and Valoroso et al. (2017). Then, to assess the time and space interaction during these two periods, we discretize the seismicity in space using 1 km bins along depth, as well as along strike. Finally, for each bin we count the number of events occurring in each time bin of 1-hr.

We start by evaluating the spatial population dynamics (Bjørnstad et al., 1999), to retrieve synchronous populations of earthquakes. To that scope, we compute the zero-lag cross-correlation (ZCC) between the event count time series defined above (Figures 5a and 5b). The resulting ZCC is expected to be high for time series having similar time evolution, thus indicating synchronous activation over different space bins (Bjørnstad et al., 1999; Frank et al., 2016; Trugman et al., 2015; Wu et al., 2015).

Figure 5a shows the results of our analysis, for the pre-swarm period. Here, small ZCC off the diagonal are observed for the full depth range, suggesting marginal spatial interaction. A similar behavior is observed for the along strike interaction (Figure 5d). On the other hand, during the swarm period we observe a systematic increase of space synchronization both in depth (Figure 5b) and along strike (Figure 5e). During the swarm period, we additionally observe that the synchronization is reduced at depths of ~ 7 km, indicating a less spatially clustered seismicity (Figure 5b). This depth limit is also associated with the base of the Mesozoic carbonates and Triassic evaporitic rocks (Chiaraluce et al., 2007; Piana Agostinetti et al., 2017; Piccinini et al., 2003). It is worth mentioning here that the seismicity below 7 km depth, mainly consists of events nucleating along the ATF volume (Figure 1).

We further assess the time interaction of the seismicity along depth, considering a point process formalism (Lowen & Teich, 2005), and the autocorrelations of the event count time series. If the auto-correlation function exhibits a distinct pulse at zero lag-time, the seismicity is temporally unrelated as expected for a Poisson process like random seismicity (Lowen & Teich, 2005). On the other hand, a smooth drop of the auto-correlation function indicates an auto-regressive model, in which the time of future earthquakes is related to the previous ones (Lowen & Teich, 2005). Figure S4a in Supporting Information S1 shows the auto-correlation functions along depth for the pre-swarm period. Here the pulse at zero lag-time indicates Poissonian-like evolution of seismicity over the entire depth range. For the swarm period (Figure S4b in Supporting Information S1), we again distinguish two behaviors. The shallow seismicity (above 7 km depth) is characterized by an auto-correlation function with a smooth decay around zero lag-time, indicating a significant time interaction. On the other hand, for the deeper part, below 7 km, the auto-correlation functions show a zero-lag pulse, as seen for the entire depth range in the pre-swarm period (Figure S4 in Supporting Information S1).

We additionally explore the time interaction of the seismicity occurring in each space bin (Figure 5c and 5f), by calculating the coefficient of variation (COV) of the interevent times. The COV provides insightful information about the time clustering of earthquakes (e.g., Cabrera et al., 2022; Kagan & Jackson, 1991; Sánchez-Reyes

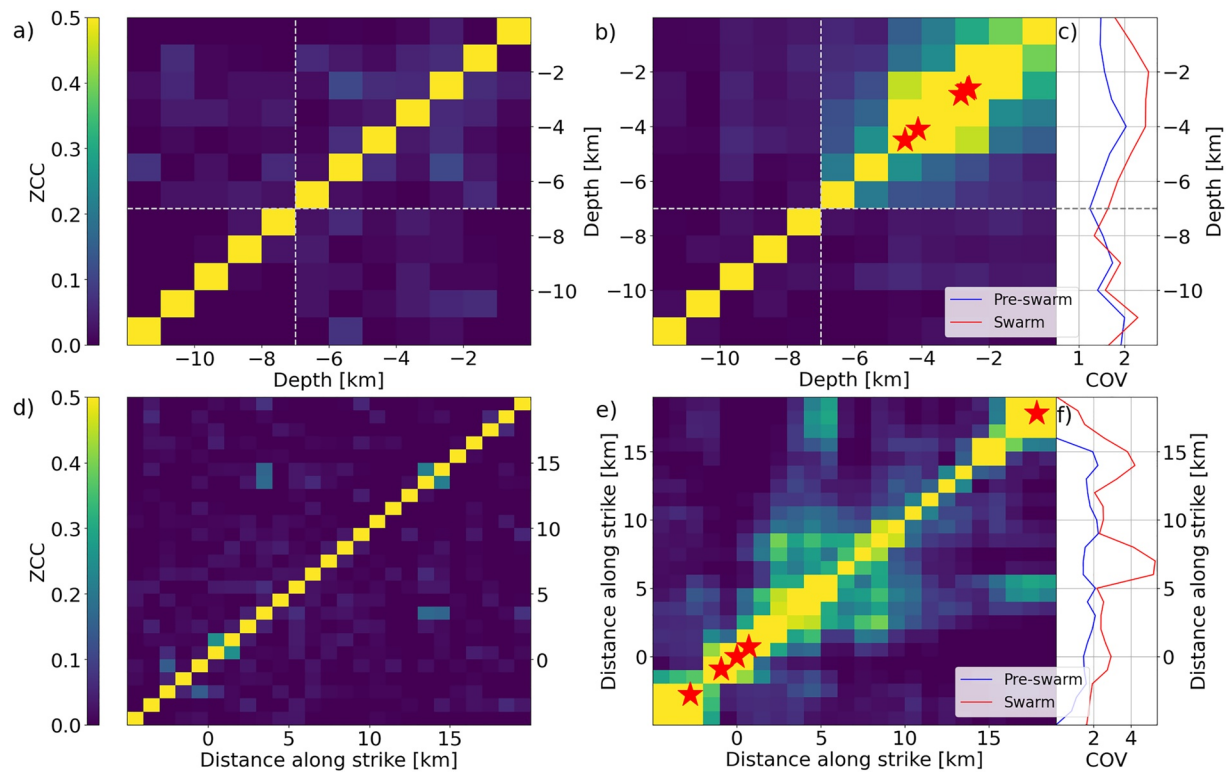


Figure 5. Pairwise zero-lag cross-correlation (ZCC) between the event count time series binned in 1 km along depth and 1-hr lasting time bins for (a) the pre-swarm and (b) the swarm time period. Red stars indicate the largest events of the sequence. (c) Coefficient of variation (COV) of the interevent times for 1 km depth bins for the pre-swarm (blue) and the swarm (red) period. In (a), (b), and (c) the dashed gray lines indicate the separation depth for Section 4.2. (d) Pairwise ZCC between the event count time series binned in 1 km along strike and 1-hr lasting time bins for the pre-swarm and (e) the swarm time period. Red stars indicate the largest event of the sequence. (f) As (c), for along strike bins.

et al., 2021; Schoenball & Ellsworth, 2017). A COV of ~ 1 indicates a Poissonian-like distribution of the interevent times while a COV > 1 indicates temporal clustering, indicative of high interaction between events. Note that for this step we employ the same time separation (before and during the swarm) applied in the previous approach but use the interevent time of events in different depth bins, thus exploring the time clustering at time scales even smaller than 1-hr.

Figure 5c shows the COV over the depth bins for the pre-swarm period (blue line) and the swarm period (red line). Over the whole depth range, the pre-swarm period exhibits quasi stable values less than 2. For the swarm period, we can distinguish between two different regimes. The shallow part above 7 km exhibits values larger than two indicating an enhanced interaction between events. However, the deeper part below 7 km remains at pre-swarm values.

The COV along strike is generally higher during the swarm phase (Figure 5f). Furthermore, during the swarm period (Figure 5f), the COV is particularly large for regions also showing significant spatial clustering (Figures 5e and 5f).

In summary, the spatio-temporal analysis reveals a strong interaction in time and space (Figure 5; Figure S4 in Supporting Information S1) occurring during the swarm period. This clustering is observed to decay as function of depth, with seismicity deeper than ~ 7 km, nucleating along the low angle normal, beginning to be less clustered in time and space (Figure 1; Figures 5a–5c).

4.2. Temporal Behavior of Template Families

We further focus on the characteristics of event families. Similar to previous studies (e.g., Cochran et al., 2018; Shelly & Johnson, 2011), a family is defined as a group of earthquakes detected by a template. From Figure 2b it is visible that the normalized waveforms of new detections within a family share similar features with their

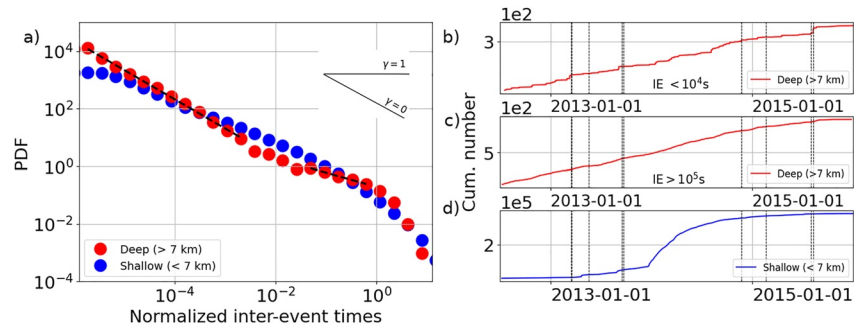


Figure 6. (a) Probability density function for the normalized interevent times of deep (red) and shallow (blue) template families. Dashed black lines indicate the least squares polynomial fit for the indicated areas. (b)–(d) Cumulative number for events for different areas and interevent times (IE). Vertical dashed lines indicate the origin times of repeating earthquakes (Section 4.3).

template. This indicates qualitatively the spatial proximity of the events belonging to a particular family. To further quantify the distances between events within a family, we take advantage of the redundant events reported in Section 2. We therefore consider events which were used as templates, and at the same time detected by other templates. As for these templates we know the precise location, we can calculate the hypo-central distances between the location of the auto-detection (i.e., a template detects the event which it was extracted from) and the locations of all additional templates, which detected this particular event. From the distances, we obtain a first order estimate of the volume a template is sensitive to. We perform this analysis for 2,052 cases of redundant detections which corresponds to ~5% of the catalog (Figure S5 in Supporting Information S1). Figure S5 in Supporting Information S1 shows that in certain rare circumstances, templates located up to 3 km away from another event may still detect it. However, ~80% of the redundant events have distances smaller than 1 km to the template. We therefore assume that hypo-central distances between events and their detecting template can be expected to be approximately 1 km. This leads us to the consideration that a family of events allows us to probe the time evolution of asperities that are close to each other, in a localized zone of the fault (e.g., Cochran et al., 2018).

Guided from the results of Section 4.1, we study in more details the properties of families in the shallow (<7 km) and deeper (>7 km) fault system (Figure 1; Figure 5; Figure S4 in Supporting Information S1). We emphasize once more that this separation is guided by the change in spatial and temporal clustering that we resolved (Figure 5; Figure S4 in Supporting Information S1), and isolate events along the low angle normal fault (>7 km, Figure 1) from earthquakes occurring both along the low angle normal fault and along high angle syn- and anti-thetic faults (<7 km, Figure 1).

For each family, we estimate the interevent times, and normalize them by the total duration of each family. The resulting normalized interevent times (τ) are then sorted within logarithmic time bins and counted. We account for logarithmic spacing, by dividing the number of normalized interevent times per bin by the length of the bin and the total number of normalized interevent times (Duverger et al., 2018). This processing provides the interevent time distributions for the two distinct depth range, as shown in Figure 6a. Their general shape can be described with a truncated gamma distribution:

$$\rho(\tau) = C(\tau)^{\gamma-1} \cdot e^{-\frac{\tau}{\beta}} \quad (1)$$

where C and β are constant while γ indicates the time clustering of the seismicity (Hainzl et al., 2006). For $\gamma = 1$ the seismicity is Poissonian-like and therefore occurs randomly in time, while for $\gamma = 0$ it follows a power-law decay similar to an Omori-like sequence (Duverger et al., 2018; Omori, 1894; Poli et al., 2022).

For families of the shallow part (above 7 km depth; Figure 6a) the interevent times linearly decay over four orders of time magnitude and can be fitted (Equation 1) with $\gamma \sim 0.26$. This value of γ is indicative of seismicity clustered in time (Duverger et al., 2018; Poli et al., 2022), but differs from classic aftershock sequence (e.g., Omori, 1894). The influence of different separation depths can be seen in Figure S7 in Supporting Information S1.

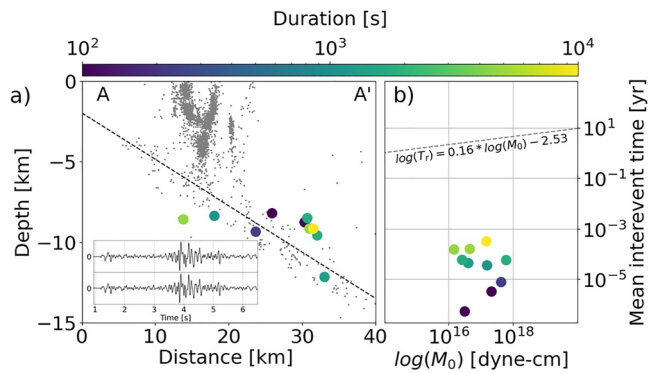


Figure 7. (a) Cross section of the ATF as seen in Figure 1b. Gray dots indicate the seismicity in vicinity to the cross section while the LAMF model is indicated as a dashed line. Color-coded dots indicate the locations and the durations of the found families of similar events. The inset shows one event pair with highly similar waveforms (waveforms of all found event families can be seen in Figure S8a-j in Supporting Information S1). (b) Mean interevent times as a function of seismic moment. In order to compare this relationship to other regions we normalized the mean interevent times by loading rates between California and the study area (Chen et al., 2007; Uchida, 2019). Dashed line indicates the interevent times expected for a loading rate of 1.7 mm/yr. Color-coded dots as in (a).

For the deep families (below 7 km depth; Figure 6a) we observe a clear change of the slope at $\tau \sim 10e - 2$. This change of the slope is indicative of a bi-modal behavior of the seismicity, similarly to the observations of Thomas et al. (2018) for low frequency earthquakes (LFE). More in particular, for $\tau < 10^{-2}$ the distribution decays with $\gamma = 0$, indicative of an Omori-like process (Omori, 1894). On the other hand, for $\tau > 10^{-2}$ the seismicity becomes less time clustered, with $\gamma = 0.55$.

To visualize the behavior of distinct time clustering discussed above, in Figures 6b–6d we show the cumulative number as function of time, for the deep and shallow seismicity. We therefore separate the seismicity of the deep families according to their absolute interevent times (short ($<10^4$ s) and long ($>10^5$ s) interevent times, Figure S6 in Supporting Information S1). We can clearly see that the temporal clustering shown in Figure 6a is mostly associated with the intermittent occurrence of quick bursts of deep seismicity with short interevent time intervals (Figure 6b). In contrast to that, the seismicity with long interevent time intervals evolves with a nearly constant rate for the whole duration of our study period (Figure 6c). After the increase in occurrences in January 2014, the seismicity associated with shallow families decays in time, following an Omori law, without however being governed by a large mainshock (Figure 6d), similar to observations of other swarms (Poli et al., 2022).

4.3. Repeating Earthquakes (RE) Along the LANF

One of the proposed mechanisms for explaining the accommodation of the extension inside the study area is gradual creep along the LANF (Anderlini et al., 2016; Vadacca et al., 2016). Creeping faults are widely recognized for producing RE: earthquakes with waveforms that are remarkably similar, radiated from asperities that are brought to failure by the loading caused by creep in the surrounding area (Nadeau & McEvilly, 1999). RE have been observed along the ATF (Chiaraluca et al., 2007), with recurrence times ranging from seconds to minutes (Valoroso et al., 2017), and are thought to be the result of creep (Anderlini et al., 2016). Several studies, however, have found that RE with short recurrence times are difficult to link to creep (Chen et al., 2013; Lengliné & Marsan, 2009).

In this work, we systematically search for REs along the LANF (seismicity below 7 km) as evidence of creep, by correlating the waveforms of events. We follow the approach of Duverger et al. (2018) and estimate the similarity value between event pairs over the entire station network, while considering the SNR of each component. It is worth mentioning that here we limit our analysis only on waveform similarities, without any attempt to relocate highly similar events (Uchida & Bürgmann, 2019).

For each pair of events with a hypo-central distance of less than 750 m in between, we extract the waveforms on all 12 components and cut it into 9.5 s lasting windows (sampled at 500 Hz) starting with the p-arrival and including substantial portions of the s-coda (Figure 7a inset). The waveforms are filtered between 1.5 and 15 Hz (Duverger et al., 2018; Schaff & Waldhauser, 2005). The upper frequency is chosen to limit the effects of different source properties, that is, changes in stress drops and thus corner frequencies (Uchida, 2019). For every detection we estimate the SNR within a 0.5 s window before the P-arrival. We cross-correlate the waveforms component-wise and extract the maximum of the resulting cross-correlation function. This maximum is then averaged over the station network while values extracted from components with a low SNR are down weighted with a logistic function (Duverger et al., 2018, Equation 1 in supplementary material).

Next, we group events sharing a similarity value (>0.95) following a simple equivalence class approach (i.e., if event A and B share a high similarity value, they open a family, if an additional event C shares a high similarity value with only one of the events A or B, it is grouped into that family).

This approach leads to 10 event families of similar events (Figure 7; Figure S8; Table S2 in Supporting Information S1). The families consist of 2–3 events, with short recurrence times of seconds to hours (Figure 7b; Table S2 in Supporting Information S1), in agreement with previous studies (Valoroso et al., 2017). From Figure 6d it

is clear that families occur unrelated to the starting time of the swarm-like seismic sequence in the shallow part of the HW, while some of them seem to be correlated in time with the short duration bursts observed from the short-lasting template families (Figure 6b).

To assess if the behavior of RE can be reconciled with fault creep (Anderlini et al., 2016), we make use of the scaling relationship between moment (M_0) and recurrence time (T_r):

$$T_r \propto M_0^{\frac{1}{6}} \quad (2)$$

proposed by Nadeau and Johnson (1998) for the San Andreas fault. In order to scale the recurrence time (T_r^{nor}) to the creep observed in the ATF, we use the normalization from Chen et al. (2007), which was shown valid over many tectonic environments:

$$T_r^{nor} = T_r (V_f / V_{parkfield}) \quad (3)$$

In this study we use 2.3 cm/yr for $V_{parkfield}$ (Uchida, 2019) while 0.17 cm/yr represents the geodetic rate of the study area (V_p , Anderlini et al., 2016).

The observed interevent times are several orders of magnitude smaller than the expected interevent times for constant creep of 0.17 cm/yr (Anderlini et al., 2016), highlighting that the RE observed along the LANF are not necessarily driven by creep, as speculated in other studies (Anderlini et al., 2016; Valoroso et al., 2017).

5. Discussion

From the study of spatial and temporal clustering of earthquakes along the ATF, we highlighted different styles of seismicity (Figure 5; Figure S4 in Supporting Information S1). Deep seismicity (depth >7 km) which includes only events nucleating along the LANF, exhibits marginal space clustering (Figure 5; Figure 6). Additionally, it is characterized by a bimodal time evolution, with short temporally clustered (Figure 6b) and long and non-temporally clustered (Figure 6c) seismicity. This result differs from a recent study (Vuan et al., 2020) which found the occurrence of swarms along the LANF as a function of activity within the HW.

At shallow depth (<7 km), the Mesozoic carbonates and Triassic evaporitic rocks (Piana Agostinetti et al., 2017) host clustered seismicity in time and space (Figure 5; Figure 6), which coincides in space with the aseismic deformation signal observed by Gualandi et al. (2017).

We here discuss in more details the different types of seismicity and the possible physical processes governing them.

5.1. The Shallow Seismicity

Shallow seismicity (depth <7 km) is radiated by syn- and antithetic high angle normal faults (above the LANF, Valoroso et al., 2017), with notably high event rates only during the time period in which Gualandi et al. (2017) observed an aseismic deformation signal at 0–5 km depth. This seismicity exhibits significant spatial clustering, which implies a simultaneous activation of large fault portions of up to 4 km in depth and of up to 5–10 km along strike, over the time scale of 1 hr (Figures 5b and 5e).

The analysis of the interevent times (Figure 6a) and the time evolution of cumulative events (Figure 6d) reveal that the swarm seismicity mimics an Omori-like sequence, without however any clear large mainshock controlling this behavior. Additionally, $\gamma \sim 0.26$, obtained from Equation 1, does not support the hypothesis of stress transfer from large events to govern the evolution of the seismicity (Duverger et al., 2018; Poli et al., 2022).

The local space and time clustering can be controlled by elastic interaction and afterslip, which play a substantial role even for small magnitude seismicity (Fattahi et al., 2015; Helmstetter et al., 2005). However, the observed rapid (1-hr) synchronization of seismicity is in many cases not associated with $M_w > 3$ earthquakes (Figure 5e) and difficult to reconcile with stress transfer or afterslip (Freed, 2005; Perfettini & Avouac, 2004). Even in the presence of $M_w > 3$ earthquakes capable of generating significant afterslip (Fattahi et al., 2015), the seismicity here is spatially synchronized on a length scale of up to 5–10 km (Figure 5). According to earthquake scaling

relations (Mai & Beroza, 2000; Wells & Coppersmith, 1994), this is 5–10 times larger than the fault size expected for the largest events in the sequence.

The large-scale interactions (Figure 5) are more similar to observed spatial and temporal synchronization described by numerical models of seismicity in complex fault systems, where it is related to positive feedback in between seismicity and creep (Cattania & Segall, 2021; Dublanchet et al., 2013).

The synchronization (Figure 5) observed for the shallow seismicity, is also similar to the behavior of LFEs observed in subduction or transform faults, during slow slip events (Frank et al., 2016; Tan & Marsan, 2020). We thus infer that the shallow seismicity can directly be used to assess the detailed spatio-temporal evolution of transient aseismic slip, not resolvable by daily geodetic measurements (Gualandi et al., 2017). Our interpretation further implies that the reported transient aseismic deformation is similar to the one observed in subduction zones. In our study area however, the distinct rheology of the shallow normal faults (Piana Agostinetti et al., 2017), as well as lower temperature and pressure values do not permit the occurrence of tremors or LFE, but rather of regular seismicity.

Interestingly, the space and time clustering occur only during the aseismic deformation episode (Gualandi et al., 2017) (Figures 5c and 5f; Figure 6; Figure S4b in Supporting Information S1), similarly to what is observed for LFE (Frank et al., 2016; Tan & Marsan, 2020). If stress transfer or afterslip from small events (Fattahi et al., 2015; Helmstetter et al., 2005) were the only factor controlling the spatial or temporal synchronization on larger scales, this effect should be observable on a smaller scale for the seismicity outside of the swarm period, contrary to what we describe (Figure 5; Figure S4 in Supporting Information S1).

The strong interactions observed (Figure 5; Figure S4 in Supporting Information S1) also suggest the complexity of the fault system, which likely consists of groups of asperities along faults, or complex fracture networks in a fault volume (Dublanchet et al., 2013). In both cases, the resulting complex rheology is likely to inhibit the propagation of large magnitude earthquakes in the shallow syn- and antithetic faults (Dublanchet et al., 2013).

Finally, we note that the absence of interaction during time periods outside of the transient aseismic deformation episode (Figure 5; Figure S4 in Supporting Information S1) indicates a mostly coupled fault system within the shallow part of the study area, which is in good agreement with the results of Anderlini et al. (2016).

5.2. The Deep Seismicity

At depths below 7 km, there is a significant change in seismicity style, with no large-scale spatial interaction (Figure 5) and much less apparent temporal interaction (Figure 5c; Figure S4 in Supporting Information S1), both independent of the 2014 transient aseismic deformation episode (Gualandi et al., 2017). This observation indicates that the deeper part of the study area, related to the LANF, is not activated during the transient aseismic deformation episode (Gualandi et al., 2017) differently from what was discussed by Vuan et al. (2020).

We additionally observe that the deep seismicity follows a bimodal time evolution, with a small number of fast reoccurring events ($<10^4$ s) exhibiting temporal interaction (Figure 6a, b), and a larger number of events exhibit long-lasting reoccurring times ($>10^5$ s) in a nearly constant time evolution (Figures 6a and 6c).

The systematic analysis of waveform similarities between events permitted to discovered 10 groups of RE. These events are used to clarify the role of creep along the ATF, in modulating their time occurrence. In Section 4.3, we utilize the scaling relationship suggested by Nadeau and Johnson (1998) and find that the interevent times do not necessarily match to the creep inferred using geodetic data (Anderlini et al., 2016, Figure 7).

Short time intervals for RE were already observed by Valoroso et al. (2017) and seem to be comparable to the short-lasting event families we report (Figures 6a and 6b). The driving mechanism of these events could therefore be stress transfer on close asperities (Chen et al., 2013; Lengliné & Marsan, 2009). To test this hypothesis, we analyze the position of the largest events within each event family (Chen et al., 2013; Lengliné & Marsan, 2009), without recognizing any clear sign of mainshock aftershock behavior (Figure S9 in Supporting Information S1).

The rapid recurrence of RE could be linked to the significant amount of high pore-fluid pressure observed in the ATF fault system (Piana Agostinetti et al., 2017). Following the model of Baisch and Harjes (2003), multiple failures of the same asperity can occur for an increase of fluid pressure. These events (Figure 7) could thus represent a mode of rupture, fully driven by short lasting (10–1,000 s) pore pressure changes, as suggested by

Collettini (2002). A simplified calculation of the pore pressure change can be done by dividing the cumulative stress drop for each family and assuming a coefficient of friction of 0.6 (Baisch & Harjes, 2003; Cochran et al., 2018). For a stress drop of 3 MPa, we obtain 10–15 MPa of pore pressure change over times ranging from ~10 to 1,000 s.

Together with the short bursts of events along the LANF (Figure 6c), we observe the occurrence of long-term and nearly continuous seismicity. This seismicity seems to agree with creep (Liu et al., 2022), as proposed by Anderlini et al. (2016). However, unlike many other well-instrumented creeping faults (e.g., Nadeau & McEvelly, 1999; Uchida, 2019; Uchida & Bürgmann, 2019), we found no evidence of RE sequences (Figure 7). This could be explained with general RE models (Chen et al., 2007; Nadeau & Johnson, 1998), despite geological studies define the LANF as a continuously deforming ductile matrix with embedded lenses of competent material that represent seismically active asperities (Collettini et al., 2011). This model would thus predict the existence of RE, with the re-rupture of asperities driven by long term creep (Chen et al., 2007; Nadeau & Johnson, 1998).

However, it should be noted that in such a fault model (Collettini et al., 2011) the role of heterogeneities in a large fault zone, can have an important role in controlling strain rate variability in space (Collettini et al., 2011; Fagereng & Sibson, 2010), and thus alter how RE occur. Thus, the lack of observed RE earthquakes can be only apparent, and result from the inaccuracy of the simple planar fault model used to predict the recurrence time (Figure 7, Chen et al., 2007). A better understanding of fault properties, strain rate distribution and their control on eventually RE is hence required to better infer the role of creep (if any) along the Alto Tiberina LANF, and LANFs in general.

Alternatively, the lack of REs might challenge the creep model proposed for the Alto Tiberina LANF (Anderlini et al., 2016). In this case alternative models that explain the observed surface displacement should be considered (Cianetti et al., 2008; Lambotte et al., 2014; Le Pourhiet et al., 2003). For example, a non-elastic volume at depth would concentrate the elastic strain upwards and produce similar surface displacement as observed for a creeping low angle fault (Lambotte et al., 2014). High temperatures can cause materials to become less viscous or plastic, which may be one of the reasons of the volume's origin (Lambotte et al., 2014). Within the study area, high temperatures could be the effect of rising CO₂ from the subducted mantle which is over-pressurized as it is trapped below the LANF (Chiodini et al., 2004). In this proposed model, the LANF accommodates little, if any deformation. Strain below the LANF would cause the continuous seismicity that we report (Cianetti et al., 2008).

6. Conclusion

By applying TM processing (Beaucé et al., 2018; Gibbons & Ringdal, 2006) to data recorded at an array of borehole stations we were able to produce a catalog of 443,677 earthquakes, expanding by ~12 times the number of events within the initial catalog (Valoroso et al., 2017). The new seismic catalog is complete to magnitude down to -0.67 .

While TM is powerful to detect many more events with low SNR, no objective method can be used to define a good and time consistent detection threshold. We therefore performed several quality controls on the detected signals to ensure to have a minimal impact of false detections in the extended catalog. With the presented approach we significantly improved the detection of small events, being able to detect earthquakes with magnitude as low as -2 (Figure 4). The extended catalog is available in electronic format (see Data Availability Statement).

The detailed analysis of this catalog enabled the identification of several types of seismicity in different parts of the fault system. We initially observe marginal temporal and spatial clustering along the whole fault system outside of the aseismic deformation episode (Figures 5a and 5d; Figure S4a in Supporting Information S1). The shallow seismicity then begins to be strongly clustered in time and space, coinciding with the 2014 aseismic deformation episode (Gualandi et al., 2017). We propose that the enhanced interaction of seismicity reflects the complexity of the slip process during the transient (Cattania & Segall, 2021; Dublanchet et al., 2013).

In the deeper part of the fault system, along the LANF, we observe bi-modal seismicity (Figure 6), with long and nearly continuous families of events, and short bursts with duration of less than 1 day. We further identified and modeled REs and illustrate the marginal role of creep in controlling their occurrence (Figure 7). We thus proposed rapid changes of pore pressure as driver of RE, which is in good agreement with geological studies (Collettini, 2002).

Finally, we show that RE are not a direct expression of creep and provide an alternative deformation model for the extension within the study area. This emphasizes that more seismo-geodetic studies are required to properly assess the deformation style occurring along the ATF during the inter-seismic periods (Anderlini et al., 2016; Vadacca et al., 2016).

Conflict of Interest

The authors declare no conflicts of interest relevant to this study.

Data Availability Statement

The extended catalog is available in electronic format at the Zenodo data set repository (<https://zenodo.org/record/6956953>). For each detected event we report the origin time, the position (which is the same as the template position), the estimated magnitude, the ID of the template detecting a given event (to group events into families) and the CC to MAD ratio. We further flag events which are human made. Different formats can be provided upon request to the authors. The continuous seismic data used in this study are available at the Istituto Nazionale di Geofisica e Vulcanologia (INGV) seismological data center (http://cnt.rm.ingv.it/webservices_and_software/, last accessed May 2021) and were downloaded using obspyDMT (Hosseini & Sigloch, 2017). For data processing we made use of the ObsPy package (Beyreuther et al., 2010; Krischer et al., 2015). The fast matched filter code was used for template matching (Beaucé et al., 2018). Computations were performed using the University of Grenoble Alpes (UGA) High-Performance Computing infrastructures CIMENT. Maps were created using the Generic Mapping Tools (GMT) version 6.0 and PyGMT (Uieda et al., 2021). Fault traces are available at the HIKE European Fault Database (v. Gessel et al., 2021). Supplemental material for this article contains nine figures, two tables and one equation, expanding the information presented in this manuscript.

Acknowledgments

This research received funding from the European Research Council (ERC) under the European Union Horizon 2020 Research and Innovation Program (grant agreements 802777- MONIFAULTS). The authors thank Glenn Cougoulat and GRICAD Grenoble Alpe Research - Scientific Computing and Data Infrastructure for their kind support during the computational part of this work. We thank Nicola D'Agostino for insightful discussions. We further thank the editor Satoshi Ide, the associate editor Patricia Martínez-Garzón, James Biemiller and two anonymous reviewers for their comments that helped to improve the manuscript.

References

- Abercrombie, R. E. (2021). Resolution and uncertainties in estimates of earthquake stress drop and energy release. *Philosophical Transactions of the Royal Society A*, 379(2196), 20200131. <https://doi.org/10.1098/rsta.2020.0131>
- Abers, G. A., Mutter, C. Z., & Fang, J. (1997). Shallow dips of normal faults during rapid extension: Earthquakes in the Woodlark-D'Entrecasteaux rift system, Papua New Guinea. *Journal of Geophysical Research*, 102(B7), 15301–15317. <https://doi.org/10.1029/97jb00787>
- Anderlini, L., Serpelloni, E., & Belardinelli, M. E. (2016). Creep and locking of a low-angle normal fault: Insights from the Altoiberina fault in the northern Apennines (Italy). *Geophysical Research Letters*, 43(9), 4321–4329. <https://doi.org/10.1002/2016gl068604>
- Baisch, S., & Harjes, H. P. (2003). A model for fluid-injection-induced seismicity at the KTB, Germany. *Geophysical Journal International*, 152(1), 160–170. <https://doi.org/10.1046/j.1365-246x.2003.01837.x>
- Barchi, M., Minelli, G., Magnani, B., & Mazzotti, A. (2003). *LXII*(62), 127–136.
- Beaucé, E., Frank, W. B., Paul, A., Campillo, M., & Van der Hilst, R. D. (2019). Systematic detection of clustered seismicity beneath the South-western Alps. *Journal of Geophysical Research: Solid Earth*, 124(11), 11531–11548.
- Beaucé, E., Frank, W. B., & Romanenko, A. (2018). Fast matched filter (FMF): An efficient seismic matched-filter search for both CPU and GPU architectures. *Seismological Research Letters*, 89(1), 165–172.
- Beyreuther, M., Barsch, R., Krischer, L., Megies, T., Behr, Y., & Wassermann, J. (2010). ObsPy: A Python toolbox for seismology. *Seismological Research Letters*, 81(3), 530–533. <https://doi.org/10.1785/gssrl.81.3.530>
- Biemiller, J., Boulton, C., Wallace, L., Ellis, S., Little, T., Mizera, M., ., & Lavier, L. (2020). Mechanical implications of creep and partial coupling on the world's fastest slipping low-angle normal fault in southeastern Papua New Guinea. *Journal of Geophysical Research: Solid Earth*, 125(10), e2020JB020117. <https://doi.org/10.1029/2020jb020117>
- Bjørnstad, O. N., Ims, R. A., & Lambin, X. (1999). Spatial population dynamics: Analyzing patterns and processes of population synchrony. *Trends in Ecology & Evolution*, 14(11), 427–432.
- Boncio, P., Brozzetti, F., & Lavecchia, G. (2000). Architecture and seismotectonics of a regional low-angle normal fault zone in central Italy. *Tectonics*, 19(6), 1038–1055. <https://doi.org/10.1029/2000tc900023>
- Byerlee, J. (1978). Friction of rocks. In *Rock friction and earthquake prediction* (pp. 615–626). https://doi.org/10.1007/978-3-0348-7182-2_4
- Cabrera, L., Poli, P., & Frank, W. B. (2022). Tracking the spatio-temporal evolution of foreshocks preceding the Mw 6.1 2009 L'Aquila earthquake. *Journal of Geophysical Research: Solid Earth*, 127(3), e2021JB023888. <https://doi.org/10.1029/2021jb023888>
- Cattania, C., & Segall, P. (2021). Precursory slow slip and foreshocks on rough faults. *Journal of Geophysical Research: Solid Earth*, 126(4), e2020JB020430. <https://doi.org/10.1029/2020jb020430>
- Chen, K. H., Bürgmann, R., & Nadeau, R. M. (2013). Do earthquakes talk to each other? Triggering and interaction of repeating sequences at Parkfield. *Journal of Geophysical Research: Solid Earth*, 118(1), 165–182. <https://doi.org/10.1029/2012jb009486>
- Chen, K. H., Nadeau, R. M., & Rau, R. J. (2007). Towards a universal rule on the recurrence interval scaling of repeating earthquakes? *Geophysical Research Letters*, 34(16). <https://doi.org/10.1029/2007gl030554>
- Chiarabba, C., & Amato, A. (2003). Vp and Vp/Vs images in the Mw 6.0 Colfiorito fault region (central Italy): A contribution to the understanding of seismotectonic and seismogenic processes. *Journal of Geophysical Research*, 108(B5). <https://doi.org/10.1029/2001jb001665>
- Chiaraluce, L., Amato, A., Carannante, S., Castelli, V., Cattaneo, M., Cocco, M., ., & Valoroso, L. (2014). The Alto Tiberina near fault observatory (northern Apennines, Italy). *Annals of Geophysics*.

- Chiaraluca, L., Chiarabba, C., Collettini, C., Piccinini, D., & Cocco, M. (2007). Architecture and mechanics of an active low-angle normal fault: Alto Tiberina fault, northern Apennines, Italy. *Journal of Geophysical Research*, 112(B10). <https://doi.org/10.1029/2007jb005015>
- Chiodini, G., Cardellini, C., Amato, A., Boschi, E., Caliro, S., Frondini, F., & Ventura, G. (2004). Carbon dioxide Earth degassing and seismogenesis in central and southern Italy. *Geophysical Research Letters*, 31(7). <https://doi.org/10.1029/2004gl019480>
- Cianetti, S., Tinti, E., Giunchi, C., & Cocco, M. (2008). Modelling deformation rates in the Western Gulf of Corinth: Rheological constraints. *Geophysical Journal International*, 174(2), 749–757. <https://doi.org/10.1111/j.1365-246x.2008.03845.x>
- Cochran, E. S., Ross, Z. E., Harrington, R. M., Dougherty, S. L., & Rubinstein, J. L. (2018). Induced earthquake families reveal distinctive evolutionary patterns near disposal wells. *Journal of Geophysical Research: Solid Earth*, 123(9), 8045–8055. <https://doi.org/10.1029/2018jb016270>
- Collettini, C. (2002). Hypothesis for the mechanics and seismic behaviour of low-angle normal faults: The example of the Altotiberina fault northern Apennines. *Annals of Geophysics*, 45(5).
- Collettini, C. (2011). The mechanical paradox of low-angle normal faults: Current understanding and open questions. *Tectonophysics*, 510(3–4), 253–268. <https://doi.org/10.1016/j.tecto.2011.07.015>
- Collettini, C., & Barchi, M. R. (2002). A low-angle normal fault in the Umbria region (central Italy): A mechanical model for the related microseismicity. *Tectonophysics*, 359(1–2), 97–115. [https://doi.org/10.1016/s0040-1951\(02\)00441-9](https://doi.org/10.1016/s0040-1951(02)00441-9)
- Collettini, C., Barchi, M. R., Chiaraluca, L., Mirabella, F., & Pucci, S. (2003). The Gubbio fault: Can different methods give pictures of the same object? *Journal of Geodynamics*, 36(1–2), 51–66. [https://doi.org/10.1016/s0264-3707\(03\)00038-3](https://doi.org/10.1016/s0264-3707(03)00038-3)
- Collettini, C., Niemeijer, A., Viti, C., Smith, S. A., & Marone, C. (2011). Fault structure, frictional properties and mixed-mode fault slip behavior. *Earth and Planetary Science Letters*, 311(3–4), 316–327. <https://doi.org/10.1016/j.epsl.2011.09.020>
- Dublanchet, P., Bernard, P., & Favreau, P. (2013). Interactions and triggering in a 3-D rate-and-state asperity model. *Journal of Geophysical Research: Solid Earth*, 118(5), 2225–2245. <https://doi.org/10.1002/jgrb.50187>
- Duverger, C., Lambotte, S., Bernard, P., Lyon-Caen, H., Deschamps, A., & Nercessian, A. (2018). Dynamics of microseismicity and its relationship with the active structures in the Western Corinth Rift (Greece). *Geophysical Journal International*, 215(1), 196–221. <https://doi.org/10.1093/gji/ggy264>
- Fagereng, Å., & Sibson, R. H. (2010). Mélange rheology and seismic style. *Geology*, 38(8), 751–754. <https://doi.org/10.1130/g30868.1>
- Fattahi, H., Amelung, F., Chaussard, E., & Wdowinski, S. (2015). Coseismic and postseismic deformation due to the 2007 M5. 5 Ghazaband fault earthquake, Balochistan, Pakistan. *Geophysical Research Letters*, 42(9), 3305–3312. <https://doi.org/10.1002/2015gl063686>
- Frank, W. B., Poli, P., & Perfettini, H. (2017). Mapping the rheology of the Central Chile subduction zone with aftershocks. *Geophysical Research Letters*, 44(11), 5374–5382. <https://doi.org/10.1002/2016gl072288>
- Frank, W. B., Shapiro, N. M., Husker, A. L., Kostoglodov, V., Gusev, A. A., & Campillo, M. (2016). The evolving interaction of low-frequency earthquakes during transient slip. *Science Advances*, 2(4), e1501616. <https://doi.org/10.1126/sciadv.1501616>
- Freed, A. M. (2005). Earthquake triggering by static, dynamic, and postseismic stress transfer. *Annual Review of Earth and Planetary Sciences*, 33, 335–367. <https://doi.org/10.1146/annurev.earth.33.092203.122505>
- Gessel, v., S., Hintersberger, E., Ede, v., R., ten Veen, J., et al. (2021). The HIKE European Fault Database (EFDB) compiled in the framework of the GeoERA project HIKE. (2018–2021). <https://doi.org/10.1002/2017jb014607>
- Gibbons, S. J., & Ringdal, F. (2006). The detection of low magnitude seismic events using array-based waveform correlation. *Geophysical Journal International*, 165(1), 149–166. <https://doi.org/10.1111/j.1365-246x.2006.02865.x>
- Gualandi, A., Nichele, C., Serpelloni, E., Chiaraluca, L., Anderlini, L., Latorre, D., et al. (2017). Aseismic deformation associated with an earthquake swarm in the northern Apennines (Italy). *Geophysical Research Letters*, 44(15), 7706–7714. <https://doi.org/10.1002/2017gl073687>
- Gulia, L., & Gasperini, P. (2021). Contamination of frequency–magnitude slope (b-Value) by Quarry Blasts: An example for Italy. *Seismological Society of America*, 92(6), 3538–3551. <https://doi.org/10.1785/0220210080>
- Hainzl, S., Scherbaum, F., & Beauval, C. (2006). Estimating background activity based on interevent-time distribution. *Bulletin of the Seismological Society of America*, 96(1), 313–320. <https://doi.org/10.1785/0120050053>
- Helmstetter, A., Kagan, Y. Y., & Jackson, D. D. (2005). Importance of small earthquakes for stress transfers and earthquake triggering. *Journal of Geophysical Research*, 110(B5). <https://doi.org/10.1029/2004jb003286>
- Herrmann, M., & Marzocchi, W. (2021). Inconsistencies and lurking pitfalls in the magnitude–frequency distribution of high-resolution earthquake catalogs. *Seismological Research Letters*, 92(2A), 909–922. <https://doi.org/10.1785/0220200337>
- Hosseini, K., & Sigloch, K. (2017). ObspyDMT: A Python toolbox for retrieving and processing large seismological data sets. *Solid Earth*, 8(5), 1047–1070. <https://doi.org/10.5194/se-8-1047-2017>
- Hreinsdóttir, S., & Bennett, R. A. (2009). Active aseismic creep on the Alto Tiberina low-angle normal fault. *Italy. Geology*, 37(8), 683–686.
- Kagan, Y. Y., & Jackson, D. D. (1991). Long-term earthquake clustering. *Geophysical Journal International*, 104(1), 117–134. <https://doi.org/10.1111/j.1365-246x.1991.tb02498.x>
- Krischer, L., Megies, T., Barsch, R., Beyreuther, M., Lecocq, T., Caudron, C., & Wassermann, J. (2015). ObsPy: A bridge for seismology into the scientific Python ecosystem. *Computational Science & Discovery*, 8(1), 014003. <https://doi.org/10.1088/1749-4699/8/1/014003>
- Lambotte, S., Lyon-Caen, H., Bernard, P., Deschamps, A., Patau, G., Nercessian, A., et al. (2014). Reassessment of the rifting process in the Western Corinth Rift from relocated seismicity. *Geophysical Journal International*, 197(3), 1822–1844. <https://doi.org/10.1093/gji/ggu096>
- Latorre, D., Amato, A., Cattaneo, M., Carranante, S., & Michelini, A. (2014). Man-induced low-frequency seismic events in Italy. *Geophysical Research Letters*, 41(23), 8261–8268. <https://doi.org/10.1002/2014gl062044>
- Lengliné, O., Frank, W. B., Marsan, D., & Ampuero, J. P. (2017). Imbricated slip rate processes during slow slip transients imaged by low-frequency earthquakes. *Earth and Planetary Science Letters*, 476, 122–131.
- Lengliné, O., & Marsan, D. (2009). Inferring the coseismic and postseismic stress changes caused by the 2004 Mw= 6 Parkfield earthquake from variations of recurrence times of microearthquakes. *Journal of Geophysical Research*, 114(B10).
- Le Pourhiet, L., Burov, E., & Moretti, I. (2003). Initial crustal thickness geometry controls on the extension in a back arc domain: Case of the Gulf of Corinth. *Tectonics*, 22(4). <https://doi.org/10.1029/2002tc001433>
- Liu, Y. K., Ross, Z. E., Cochran, E. S., & Lapusta, N. (2022). A unified perspective of seismicity and fault coupling along the San Andreas Fault. *Science Advances*, 8(8), eabk1167. <https://doi.org/10.1126/sciadv.abk1167>
- Lowen, S. B., & Teich, M. C. (2005). *Fractal-based point processes*. John Wiley & Sons.
- Mai, P. M., & Beroza, G. C. (2000). Source scaling properties from finite-fault-rupture models. *Bulletin of the Seismological Society of America*, 90(3), 604–615. <https://doi.org/10.1785/0119990126>
- Majstorović, J., Giffard-Roisin, S., & Poli, P. (2021). Designing convolutional neural network pipeline for near-fault earthquake catalog extension using single-station waveforms. *Journal of Geophysical Research: Solid Earth*, 126(7), e2020JB021566.

- Marsan, D., & Nalbant, S. S. (2005). Methods for measuring seismicity rate changes: A review and a study of how the M w 7.3 lands earthquake affected the aftershock sequence of the M w 6.1 Joshua tree earthquake. *Pure and Applied Geophysics*, 162(6), 1151–1185. <https://doi.org/10.1007/s00024-004-2665-4>
- Martínez-Garzón, P., Durand, V., Bentz, S., Kwiatek, G., Dresen, G., Turkmen, T., .. & Bohnhoff, M. (2021). Near-fault monitoring reveals combined seismic and slow activation of a fault Branch within the Istanbul–Marmara seismic gap in Northwest Turkey. *Seismological Society of America*, 92(6), 3743–3756.
- Mirabella, F., Ciaccio, M. G., Barchi, M. R., & Merlini, S. (2004). The Gubbio normal fault (central Italy): Geometry, displacement distribution and tectonic evolution. *Journal of Structural Geology*, 26(12), 2233–2249. <https://doi.org/10.1016/j.jsg.2004.06.009>
- Nadeau, R. M., & Johnson, L. R. (1998). Seismological studies at Parkfield VI: Moment release rates and estimates of source parameters for small repeating earthquakes. *Bulletin of the Seismological Society of America*, 88(3), 790–814.
- Nadeau, R. M., & McEvilly, T. V. (1999). Fault slip rates at depth from recurrence intervals of repeating microearthquakes. *Science*, 285(5428), 718–721. <https://doi.org/10.1126/science.285.5428.718>
- Obara, K. (2002). Nonvolcanic deep tremor associated with subduction in southwest Japan. *Science*, 296(5573), 1679–1681. <https://doi.org/10.1126/science.1070378>
- Omori, F. (1894). On after-shocks. *Seismological journal of Japan*, (19), 71–80.
- Pauselli, C., Barchi, M. R., Federico, C., Magnani, M. B., & Minelli, G. (2006). The crustal structure of the northern Apennines (central Italy): An insight by the CROP03 seismic line. *American Journal of Science*, 306(6), 428–450. <https://doi.org/10.2475/06.2006.02>
- Peng, Z., & Zhao, P. (2009). Migration of early aftershocks following the 2004 Parkfield earthquake. *Nature Geoscience*, 2(12), 877–881. <https://doi.org/10.1038/ngeo697>
- Perfettini, H., & Avouac, J. P. (2004). Postseismic relaxation driven by brittle creep: A possible mechanism to reconcile geodetic measurements and the decay rate of aftershocks, application to the Chi-Chi earthquake, Taiwan. *Journal of Geophysical Research*, 109(B2). <https://doi.org/10.1029/2003jb002488>
- Piana Agostinetti, N., Giacomuzzi, G., & Chiarabba, C. (2017). Seismic swarms and diffuse fracturing within Triassic evaporites fed by deep degassing along the low-angle Alto Tiberina normal fault (central Apennines, Italy). *Journal of Geophysical Research: Solid Earth*, 122(1), 308–331. <https://doi.org/10.1002/2016jb013295>
- Piccinini, D., Cattaneo, M., Chiarabba, C., Chiaraluca, L., De Martin, M., Di Bona, M., .. & Fabbri, J. (2003). A microseismic study in a low seismicity area of Italy: The Città di Castello 2000–2001 experiment. *Annals of Geophysics*.
- Pinzon-Rincon, L., Lavoué, F., Mordret, A., Boué, P., Brenguier, F., Dales, P., .. & Hollis, D. (2021). Humming trains in seismology: An opportune source for probing the shallow crust. *Seismological Research Letters*, 92(2A), 623–635.
- Poli, P., Boaga, J., Molinari, I., Cascone, V., & Boschi, L. (2020). The 2020 coronavirus lockdown and seismic monitoring of anthropic activities in Northern Italy. *Scientific Reports*, 10(1), 1–8. <https://doi.org/10.1038/s41598-020-66368-0>
- Poli, P., Cabrera, L., Flores, M. C., Báez, J. C., Ammirati, J. B., Vásquez, J., & Ruiz, S. (2022). Volcanic origin of a long-lived swarm in the Central Bransfield Basin, Antarctica. *Geophysical Research Letters*, e2021GL095447. <https://doi.org/10.1029/2021gl095447>
- Rietbrock, A., Tiberi, C., Scherbaum, F., & Lyon-Caen, H. (1996). Seismic slip on a low angle normal fault in the Gulf of Corinth: Evidence from high-resolution cluster analysis of microearthquakes. *Geophysical Research Letters*, 23(14), 1817–1820. <https://doi.org/10.1029/96gl01257>
- Ruhl, C. J., Abercrombie, R. E., Smith, K. D., & Zaliapin, I. (2016). Complex spatiotemporal evolution of the 2008 Mw 4.9 Mogul earthquake swarm (Reno, Nevada): Interplay of fluid and faulting. *Journal of Geophysical Research: Solid Earth*, 121(11), 8196–8216. <https://doi.org/10.1002/2016jb013399>
- Sánchez-Reyes, H., Essing, D., Beaucé, E., & Poli, P. (2021). The imbricated foreshock and aftershock activities of the Balsorano (Italy) Mw 4.4 normal fault earthquake and implications for earthquake initiation. *Seismological Research Letters*, 92(3), 1926–1936.
- Schaff, D. P., & Waldhauser, F. (2005). Waveform cross-correlation-based differential travel-time measurements at the Northern California Seismic Network. *Bulletin of the Seismological Society of America*, 95(6), 2446–2461. <https://doi.org/10.1785/0120040221>
- Schoenball, M., & Ellsworth, W. L. (2017). A systematic assessment of the spatiotemporal evolution of fault activation through induced seismicity in Oklahoma and southern Kansas. *Journal of Geophysical Research: Solid Earth*, 122(12), 10–189. <https://doi.org/10.1002/2017jb014850>
- Seno, T., & Yamasaki, T. (2003). Low-frequency tremors, intraslab and interplate earthquakes in southwest Japan—From a viewpoint of slab dehydration. *Geophysical Research Letters*, 30(22). <https://doi.org/10.1029/2003gl018349>
- Serpelloni, E., Anzidei, M., Baldi, P., Casula, G., & Galvani, A. (2005). Crustal velocity and strain-rate fields in Italy and surrounding regions: New results from the analysis of permanent and non-permanent GPS networks. *Geophysical Journal International*, 161(3), 861–880. <https://doi.org/10.1111/j.1365-246x.2005.02618.x>
- Shelly, D. R. (2020). A high-resolution seismic catalog for the initial 2019 Ridgecrest earthquake sequence: Foreshocks, aftershocks, and faulting complexity. *Seismological Research Letters*, 91(4), 1971–1978. <https://doi.org/10.1785/0220190309>
- Shelly, D. R., Beroza, G. C., Ide, S., & Nakamura, S. (2006). Low-frequency earthquakes in Shikoku, Japan, and their relationship to episodic tremor and slip. *Nature*, 442(7099), 188–191. <https://doi.org/10.1038/nature04931>
- Shelly, D. R., & Johnson, K. M. (2011). Tremor reveals stress shadowing, deep postseismic creep, and depth-dependent slip recurrence on the lower-crustal San Andreas fault near Parkfield. *Geophysical Research Letters*, 38(13). <https://doi.org/10.1029/2011gl047863>
- Tan, Y. J., & Marsan, D. (2020). Connecting a broad spectrum of transient slip on the San Andreas fault. *Science Advances*, 6(33), eabb2489. <https://doi.org/10.1126/sciadv.abb2489>
- Thomas, A. M., Beeler, N. M., Bletery, Q., Burgmann, R., & Shelly, D. R. (2018). Using low-frequency earthquake families on the San Andreas Fault as deep creepmeters. *Journal of Geophysical Research: Solid Earth*, 123(1), 457–475. <https://doi.org/10.1002/2017jb014404>
- Trugman, D. T., Wu, C., Guyer, R. A., & Johnson, P. A. (2015). Synchronous low frequency earthquakes and implications for deep San Andreas Fault slip. *Earth and Planetary Science Letters*, 424, 132–139. <https://doi.org/10.1016/j.epsl.2015.05.029>
- Uchida, N. (2019). Detection of repeating earthquakes and their application in characterizing slow fault slip. *Progress in Earth and Planetary Science*, 6(1), 1–21. <https://doi.org/10.1186/s40645-019-0284-z>
- Uchida, N., & Bürgmann, R. (2019). Repeating earthquakes. *Annual Review of Earth and Planetary Sciences*, 47, 305–332. <https://doi.org/10.1146/annurev-earth-053018-060119>
- Uieda, L., Tian, D., Leong, W. J., Toney, L., Schlitzer, W., Grund, M., .. & Wessel, P. (2021). PyGMT: A Python interface for the generic mapping tools.
- Vadacca, L., Casarotti, E., Chiaraluca, L., & Cocco, M. (2016). On the mechanical behaviour of a low-angle normal fault: The Alto Tiberina Fault (northern Apennines, Italy) system case study. *Solid Earth*, 7(6), 1537–1549. <https://doi.org/10.5194/se-7-1537-2016>
- Valoroso, L., Chiaraluca, L., Di Stefano, R., & Monachesi, G. (2017). Mixed-mode slip behavior of the Altotiberina low-angle normal fault system (Northern Apennines, Italy) through high-resolution earthquake locations and repeating events. *Journal of Geophysical Research: Solid Earth*, 122(12), 10–220. <https://doi.org/10.1002/2017jb014607>

- Vuan, A., Brondi, P., Sukan, M., Chiaraluze, L., Di Stefano, R., & Michele, M. (2020). Intermittent slip along the Alto Tiberina low-angle normal fault in central Italy. *Geophysical Research Letters*, *47*(17), e2020GL089039. <https://doi.org/10.1029/2020gl089039>
- Wells, D. L., & Coppersmith, K. J. (1994). New empirical relationships among magnitude, rupture length, rupture width, rupture area, and surface displacement. *Bulletin of the Seismological Society of America*, *84*(4), 974–1002.
- Wernicke, B. (1995). Low-angle normal faults and seismicity: A review. *Journal of Geophysical Research*, *100*(B10), 20159–20174. <https://doi.org/10.1029/95jb01911>
- Wu, C., Guyer, R., Shelly, D., Trugman, D., Frank, W., Gombert, J., & Johnson, P. (2015). Spatial-temporal variation of low-frequency earthquake bursts near Parkfield, California. *Geophysical Journal International*, *202*(2), 914–919. <https://doi.org/10.1093/gji/ggv194>